

Article

Insights into Cu–Amorphous Silica–Alumina as a Bifunctional Catalyst for the Steam Reforming of Dimethyl Ether

Zhi-Cui Shao, Lei Wang, Min-Li Zhu, Chang Liu  and Zhong-Wen Liu * 

Key Laboratory of Syngas Conversion of Shaanxi Province, School of Chemistry & Chemical Engineering, Shaanxi Normal University, Xi'an 710119, China

* Correspondence: zwliu@snnu.edu.cn

Abstract: The steam reforming of dimethyl ether (SRD) has been proved to be one of the most promising routes for on-site H₂ production. However, the two-step consecutive nature of the SRD reaction makes the design of an efficient bifunctional catalyst a challenge. Herein, a series of Cu incorporated into amorphous silica–alumina (Cu–ASA) as integrated bifunctional catalysts for SRD were synthesized by the single-step complex decomposition method, and ammonium carbonate was confirmed to be an effective complex agent for dispersing Cu in ASA. The results indicated that the initial conversion of dimethyl ether and a H₂ yield higher than 90% were achieved at 300 °C over the optimal catalyst. More importantly, a slightly decreased SRD performance with increasing time-on-stream was mainly caused by Cu sintering, and the synergetic effect between ASA and Cu played a crucial role in determining the activity, hydrogen yield, and stability of the integrated Cu–ASA bifunctional catalyst for SRD. These findings are helpful to develop a high-performance integrated bifunctional catalyst for the SRD reaction.

Keywords: amorphous silica–alumina; copper; bifunctional catalyst; synergetic effect; steam reforming; dimethyl ether; hydrogen production



Citation: Shao, Z.-C.; Wang, L.; Zhu, M.-L.; Liu, C.; Liu, Z.-W. Insights into Cu–Amorphous Silica–Alumina as a Bifunctional Catalyst for the Steam Reforming of Dimethyl Ether.

Catalysts **2022**, *12*, 1355. <https://doi.org/10.3390/catal12111355>

Academic Editor: Nicolas Abatzoglou

Received: 13 October 2022

Accepted: 1 November 2022

Published: 3 November 2022

Publisher's Note: MDPI stays neutral with regard to jurisdictional claims in published maps and institutional affiliations.

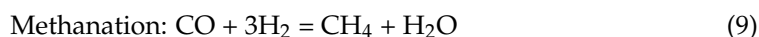
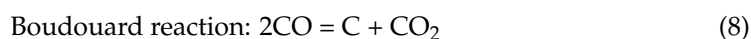
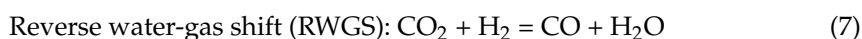
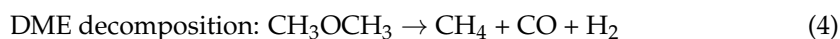
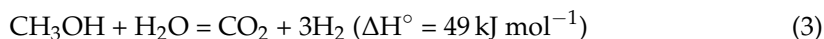
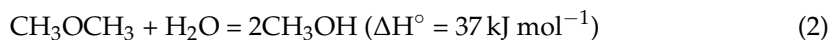


Copyright: © 2022 by the authors. Licensee MDPI, Basel, Switzerland. This article is an open access article distributed under the terms and conditions of the Creative Commons Attribution (CC BY) license (<https://creativecommons.org/licenses/by/4.0/>).

1. Introduction

Hydrogen has been revealed as one of the most efficient and clean energy carriers. However, because of the essentially secondary energy characteristics of hydrogen, important issues including its production, transport, and storage are still not well understood, and these types of studies have become hot topics in the energy-related domains. Among the potential candidates, a high hydrogen content of 13.0 wt.%, a gas-like property but liquid-storage density, and available logistics infrastructure similar to liquefied petroleum gas make dimethyl ether (DME) a competitive hydrogen carrier [1], and the steam reforming of DME (SRD, Equation (1)) is quantitatively investigated as a promising on-site hydrogen source for mobile applications such as fuel cell vehicles [1,2]. Despite this, the thermodynamic superiority of SRD compared to the steam-reforming reactions of methanol and ethanol was reported in 2000 for the first time [3]. In 2001, the exploration of the possible catalysts revealed that SRD is a two-step reaction composed of the hydrolysis of DME to MeOH (Equation (2)) and the consecutive steam reforming of the formed MeOH (SRM, Equation (3)) [4]. With this mechanistic understanding, the physical mixtures of different solid acids such as alumina [5–7] and zeolites [8,9] and the supported metals such as Cu [10,11] and noble metals [12,13] were focused on as effective bifunctional catalysts of SRD although other types of catalysts have also been reported to be active, such as Mo₂C [14]. Depending on the composition of the hybrid catalyst and reaction conditions, especially temperature, side reactions that accompany SRD, such as those in Equations (4)–(9), occur to different extents [1,5]. Thus, because of the complex reaction network and short history of the studies on the SRD reaction, it is still at the stage of catalyst

screening [15,16] although few studies on the development of reactors have been reported, such as the micro-channel reactor reported in the reference [17].



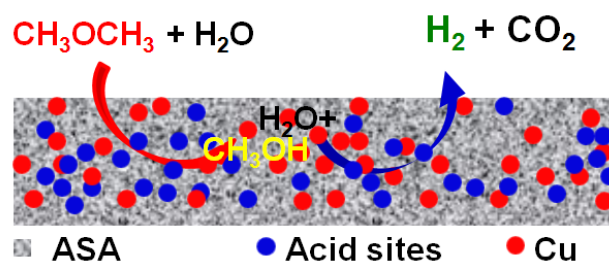
Following the two-step mechanism, an active, selective, and stable SRD catalyst composed of supported metal and solid acid is reasonably expected provided that (1) the reaction rates of the DME hydrolysis and SRM are sufficiently high; (2) the MeOH intermediate formed via DME hydrolysis can be instantaneously consumed in the subsequent SRM reaction; and (3) side reactions can be inhibited to the least extent. In the case of the metal catalysts for the SRM reaction, Cu-based catalysts are industrially promising due mainly to the reasonably high activity and relatively abundant reserves [18]. More importantly, supported Cu is revealed to be reasonably active and stable for SRM at reaction temperatures less than 300 °C [18]. Thus, for the development of a Cu-based bifunctional SRD catalyst, the solid acid must be sufficiently active for the hydrolysis of DME below 300 °C. In this case, the parent or modified zeolites with different topologies [1,8] and alumina prepared by various methods [2,6,7] are concentrated as solid acids for SRD. In fact, the amorphous silica–alumina composite (ASA) has long been commercialized for acid-catalyzed reactions in petroleum refining such as isomerization and hydrocracking [19]. Moreover, ASA with medium acidity, i.e., richer weak and medium acid sites than alumina but without the strong acid sites of zeolites, can be a suitable solid acid for SRD. This was confirmed in our previous results, in which the hybrids composed of the commercial Cu/ZnO/Al₂O₃ and ASA prepared by either the hydrolytic method [16] or the complex decomposition method [11] were effective bifunctional catalysts for SRD.

If the configuration of the bifunctional catalysts for SRD is examined, overwhelmingly reported results are achieved regarding the physical mixtures with either loosely (granular mixture) or intimately (powdery mixture) contacted states depending on the particle sizes of the component catalysts. Specifically, both the SRD activity and H₂ yield were found to be dependent on the topology and acidity of zeolites, i.e., clearly higher SRD performance for the powdery mixture of Cu/ZnO/Al₂O₃ and the HUSY zeolite compared with that of the granular mixture with the same composition vs. similar SRD performances for the granular and powdery mixtures of Cu/ZnO/Al₂O₃ and H-ZSM-5 [1]. Furthermore, the mutual effects of Cu/ZnO/Al₂O₃ and MgO-modified H-ZSM-5 on their powdery mixture were clearly manifested during the evaluation of the SRD stability of the bifunctional catalysts [15]. If the few studies on the SRD of integrated bifunctional catalysts are analyzed, e.g., mesoporous Cu–Al₂O₃ and Cu–SiO₂–Al₂O₃ prepared by the evaporation induced self-assembled method [20], Cu–ZnO–Al₂O₃ prepared by the sol–gel method [7], and Cu impregnated on different forms of γ–Al₂O₃ [6], the presence of synergetic effects between the two catalytic functions can be easily concluded, which may originate from varied structural properties and contact states of the bifunctional catalyst. Thus, as a result of the two-step consecutive nature of the SRD reaction, a deep understanding of the synergetic effects is important for the development of a high-performance bifunctional catalyst.

Based on these analyses and the easily regulated acid and textural properties of ASA, in this work, Cu–ASA with different compositions was prepared by the single-step complex decomposition method, and more attention was paid to the synergy between Cu and ASA for the SRD reaction. Results confirmed that Cu–ASA is a promising integrated bifunctional catalyst for hydrogen production via SRD, for which the initial DME conversion and H₂ yield greater than 90% were achieved at 300 °C. Importantly, the synergetic effect between Cu and ASA was revealed to play a crucial role in determining the activity, H₂ yield, and stability of the Cu–ASA bifunctional catalyst.

2. Results and Discussion

Following the two-step mechanism of the SRD reaction, the active sites of Cu–ASA as a bifunctional catalyst are acid centers for the DEM hydrolysis (Equation (2)) and metallic Cu (Cu⁰) for SRM (Equation (3)), which are illustrated in Scheme 1. Thus, the amount of Cu and the Si/Al molar ratios are optimized to understand the synergetic effects between Cu and acid sites. In this case, the catalysts are divided into two sets, i.e., the one series with varied CuO contents (10–35 wt.%) but keeping the same Si/Al molar ratio of 4 (*x*Cu–ASA-4) and the other series with the same CuO content of 25 wt.% but varied Si/Al ratios from 1 to 5 (25Cu–ASA-*y*). The results are discussed as follows together with those for 25Cu/ASA-4 as the reference catalyst.



Scheme 1. Illustrative two-step mechanism of the SRD of Cu–ASA catalysts.

2.1. Impacts of CuO Contents

Figure 1 shows the XRD patterns of calcined and reduced 25Cu/ASA-4 and *x*Cu–ASA-4 catalysts, and the particle sizes calculated based on Scherrer's formula and (111) diffractions are given in Table 1. For all of the calcined catalysts (Figure 1a), the broad peak centered at 2θ of about 23° was clearly observed, which is ascribed to amorphous silica. Noteworthy, no diffractions assigned to the crystalline phases of Al₂O₃, SiO₂, and the derived structures including the spinel were observed for all of the catalysts, which is different from those of the mesoporous Cu–Al₂O₃ and Cu–SiO₂–Al₂O₃ reported in the reference [20]. This may be reasonably explained as the relatively lower calcination temperature of 550 °C, leading to the amorphous nature of ASA. In the case of Cu species, the characteristic diffractions of CuO at 2θ of 35.5° , 38.7° , and 48.8° were clearly observed for the samples with CuO contents higher than 20 wt.%. Moreover, the intensity of the CuO peaks was apparently increased when the CuO content was increased from 25 to 35 wt.%. This was directly reflected in the accordingly increased particle size from 15 to 21 nm (Table 1), which was calculated based on the diffraction of CuO (111) at 2θ of 35.5° . Thus, the absent diffractions of Cu species for the 10Cu–ASA-4 and 20Cu–ASA-4 catalysts were reasonably attributed to their smaller sizes insensitive to XRD, indicating the highly dispersed states. If the reference catalyst prepared by the impregnation method was compared, the main diffractions of CuO at 2θ of 35.5° , 38.7° , 48.8° , 58.2° , 61.6° , 66.1° , and 67.9° were fully developed, and the particle size of CuO (28 nm) was much larger than that of 25Cu–ASA-4 (15 nm, Table 1). These results indicate the superiority of the single-step complex decomposition method for preparing highly dispersed Cu catalysts.

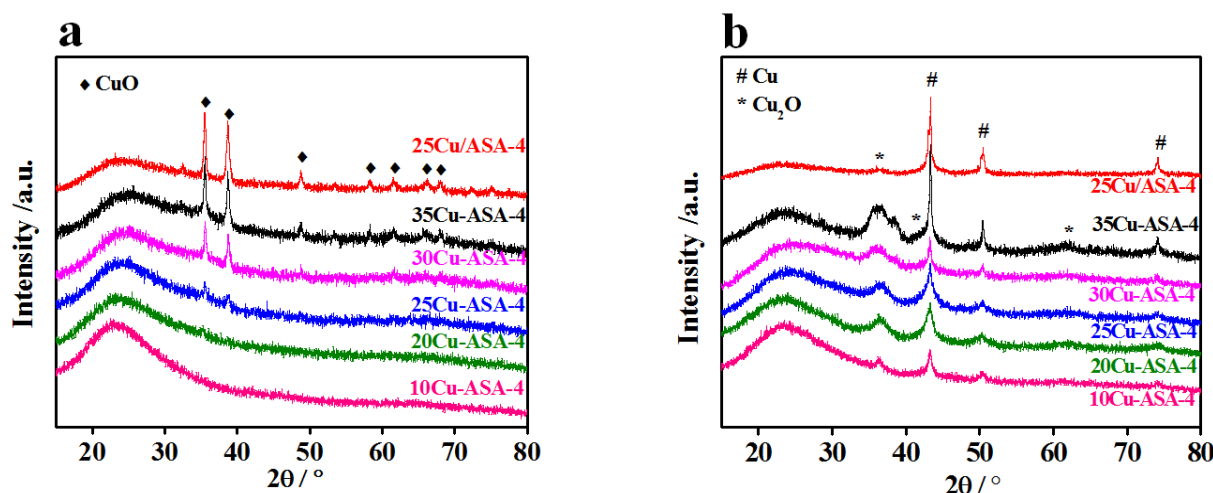


Figure 1. XRD patterns of the calcined (a) and reduced (b) $x\text{Cu-ASA-4}$ and 25Cu/ASA-4 catalysts (reduction conditions: $300\text{ }^\circ\text{C}$ for 30 min in the $10\%\text{H}_2/\text{N}_2$ mixed gases).

Table 1. Summary of the textural properties and the particle size determined by XRD for $x\text{Cu-ASA-}y$ catalysts.

Catalyst	Surface Area ($\text{m}^2 \cdot \text{g}^{-1}$)	Total Pore Volume ($\text{cm}^3 \cdot \text{g}^{-1}$)	Average Pore Size (nm)	CuO Size (nm)	Cu ⁰ Size (nm)
ASA-4	354.9	0.48	5.4	–	–
25Cu/ASA-4	–	–	–	28	35
10Cu-ASA-4	357.7	0.49	5.5	–	12
20Cu-ASA-4	282.1	0.37	5.3	–	16
25Cu-ASA-4	295.6	0.38	5.2	15	21
30Cu-ASA-4	266.9	0.38	5.7	20	27
35Cu-ASA-4	226.8	0.36	6.5	21	33
25Cu-ASA-1	252.7	0.34	5.3	22	–
25Cu-ASA-2	269.1	0.34	5.0	22	–
25Cu-ASA-3	293.2	0.39	4.9	21	–
25Cu-ASA-5	331.3	0.47	5.1	15	–

For the reduced $x\text{Cu-ASA-4}$ catalysts (Figure 1b), ASA was still amorphous as reflected in the broad XRD peak. In contrast, where the Cu species were concerned, new diffractions emerged irrespective of the CuO contents, which can be assigned to Cu_2O ($2\theta = 36.6, 42.4,$ and 61.4°) and Cu^0 ($2\theta = 43.4, 50.5,$ and 74.1°) according to the references [21,22]. Moreover, the intensity for both the Cu^0 (111) peak at 2θ of 43.4° and Cu_2O (111) diffraction at 2θ of 36.6° was gradually increased with increasing CuO content of $x\text{Cu-ASA-4}$, revealing the increased particle sizes of Cu^0 and Cu_2O . This was directly found from the calculated Cu^0 size (Table 1), i.e., from 12 nm (10Cu-ASA-4) to 33 nm (35Cu-ASA-4). Noteworthy, no Cu species were detected by XRD for the calcined 10Cu-ASA-4 and 20Cu-ASA-4 catalysts while clear XRD diffractions of Cu^0 and Cu_2O appeared for the reduced catalyst even with the lowest CuO content of 10 wt.%. This was consistent with the easy sintering of Cu species during the reduction in hydrogen although it was performed at a temperature as low as $300\text{ }^\circ\text{C}$. If the Cu^0 particle size of the reduced 25Cu/ASA-4 catalyst was examined (35 nm, Table 1), it was much larger than that of the reduced 25Cu-ASA-4 catalyst (21 nm).

With the use of 25Cu-ASA-4 as a representative, TEM was performed to directly observe the Cu species of the catalysts. For the calcined 25Cu-ASA-4 catalyst (Figure 2a), the CuO particles identified by the lattice fringe of 0.234 nm were clearly seen and were assigned to CuO (111). Moreover, the size distribution of the CuO particles was relatively narrower, and the average size was 5.3 ± 1.0 nm. When 25Cu-ASA-4 was reduced (Figure 2b), Cu (111) lattice fringes with a d-spacing of 0.212 nm were ascertained. In comparison with the

calcined catalyst, the size distribution of the Cu^0 particles was broader and the average Cu^0 particle size (5.6 ± 1.5 nm) was slightly larger. Although the change trends of the average particle sizes was consistent with that of the XRD results, they were much smaller than those calculated from the XRD diffractions.

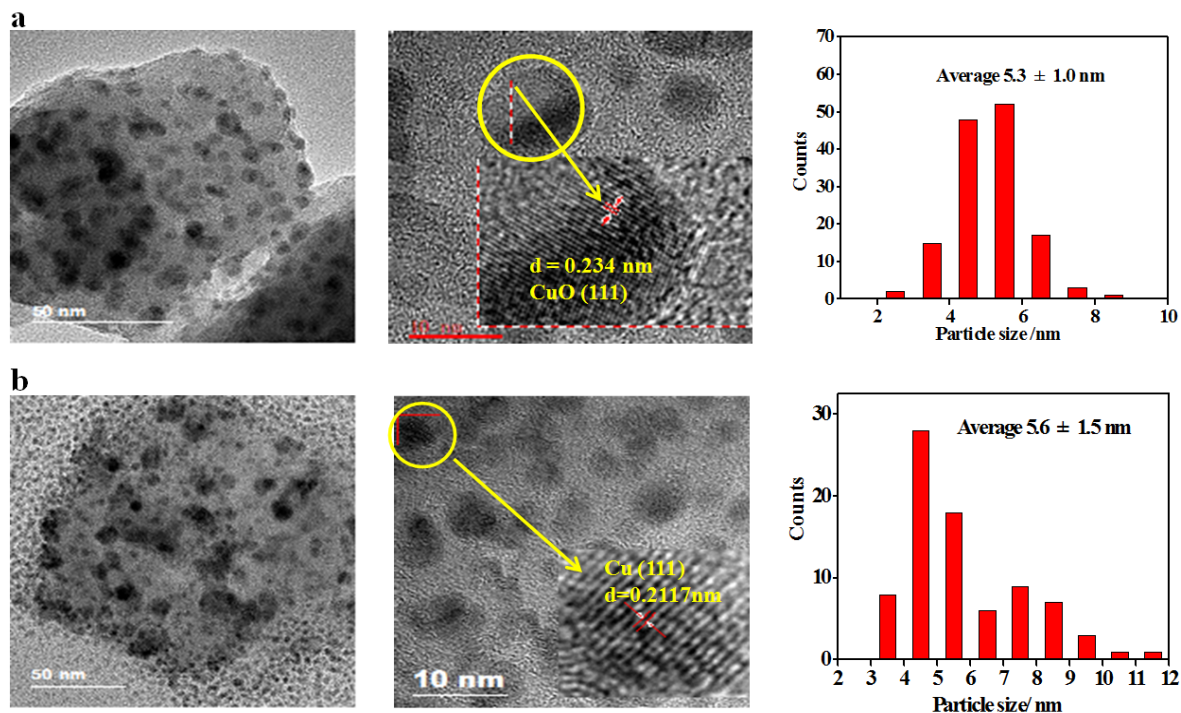


Figure 2. TEM and HRTEM images and particle size distributions of the calcined (a) and reduced (b) 25Cu-ASA-4 catalyst (reduction conditions: 300 °C for 30 min in the 10% H_2/N_2 mixed gas).

The nitrogen adsorption–desorption isotherms of the ASA-4 and $x\text{Cu}$ -ASA-4 catalysts are shown in Figure 3a. Irrespective of the samples, a type IV isotherm with a clear H3 hysteresis loop based on the IUPAC classification [23] was observed, indicating the irregular porous structure with micro-, meso-, and macropores. If the isotherms in the range of P/P_0 less than 0.05 were examined, the addition of CuO and increasing its content up to 35 wt.% led to very limited changes in the amount of adsorbed N_2 , indicating very similar micropores across all of the samples. This observation was consistent with the amorphous properties of ASA. As indicated from the calculated data (Table 1), the BET specific surface area of ASA-4 was as high as $356.3 \text{ m}^2 \cdot \text{g}^{-1}$, characterizing the superiority of the complex decomposition method in the preparation of the amorphous oxides. Moreover, even a slightly higher BET specific surface area of $357.7 \text{ m}^2 \cdot \text{g}^{-1}$ was obtained for 10Cu-ASA-4, which agrees with the high dispersion of CuO in ASA revealed in the XRD characterizations. In the cases of Cu-ASA-4 catalysts with CuO contents from 20 to 35 wt.%, the BET specific surface area, the total pore volume, and the average pore diameter were very similar and in agreement with the high dispersion of CuO in the amorphous silica–alumina composites.

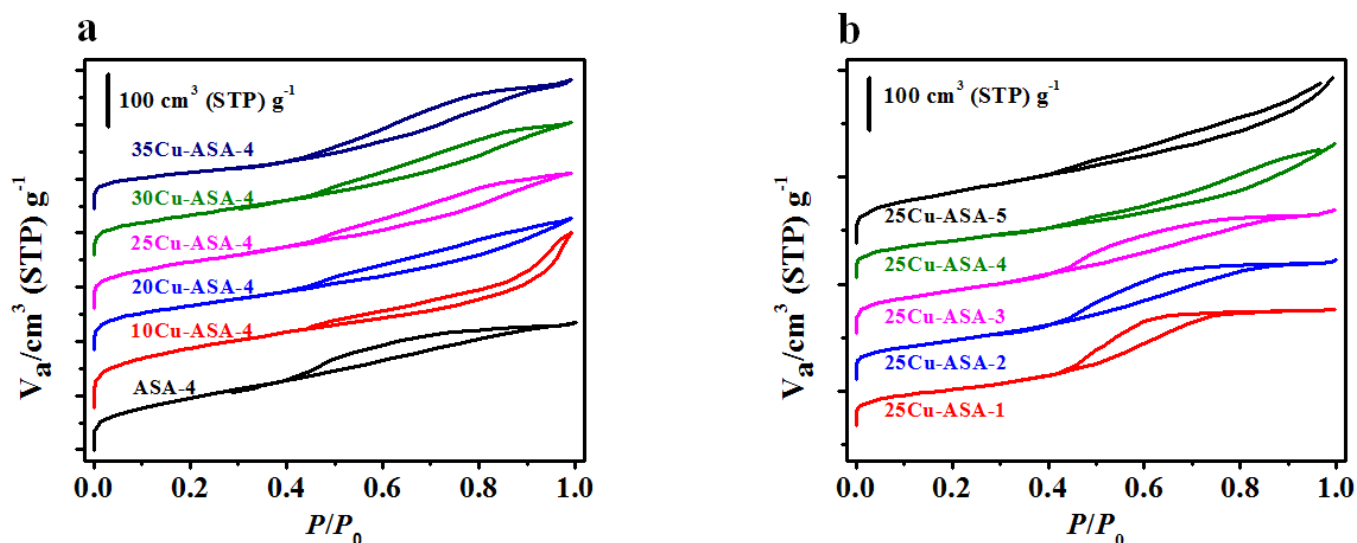


Figure 3. N₂ adsorption/desorption isotherms of $x\text{Cu-ASA-4}$ (a) and $25\text{Cu-ASA-}y$ (b) catalysts.

Figure 4 shows the reducibility of the $x\text{Cu-ASA-4}$ and 25Cu/ASA-4 catalysts. For all of the samples, only one asymmetric H₂-consumption peak centered below 300 °C was observed throughout the H₂-TPR process until 600 °C. This observation clearly indicates that the difficult reducible Cu species such as the CuAl₂O₄ spinel were not formed over all of the catalysts, which is supported by the XRD results (Figure 1a). Considering the irreducible nature of ASA, the H₂ consumption exclusively originated from the reduction of CuO, which was detected by XRD. This was further supported by the continuously increased intensity of the H₂-TPR peak with the increasing CuO content of $x\text{Cu-ASA-4}$. If the temperature at the peak maximum was examined, it continuously decreased from about 272 to ~258 °C with increasing CuO content in $x\text{Cu-ASA-4}$ from 10 to 30 wt.%. By correlating this observation with the calculated CuO particle sizes (Table 1) and XRD patterns, it can be explained as the increased difficulty for the reduction of the highly dispersed CuO with smaller sizes, which is consistent with the reference results [20,24]. This explanation was further supported by the following facts, i.e., almost the same peak temperatures (~258 °C) for 30Cu-ASA-4 and 35Cu-ASA-4 with comparable CuO sizes of 20–21 nm, and the lowest peak temperature of ~250 °C for 25Cu/ASA-4 with the largest CuO particle size (35 nm). As reported in the literature, one of the possible routes for the reduction of CuO in H₂ is the two-step process of CuO to Cu₂O and the subsequent Cu₂O conversion to Cu⁰ [25]. Thus, the asymmetry of the H₂-TPR peak may be due to the varied Cu⁰/Cu⁺ ratios of different catalysts as revealed from the XRD patterns of the reduced catalysts (Figure 1b). Alternatively, the asymmetric peak may also originate from the varied reducibility of CuO particles with different sizes as indicated from the broad size distribution over the catalyst (Figure 2).

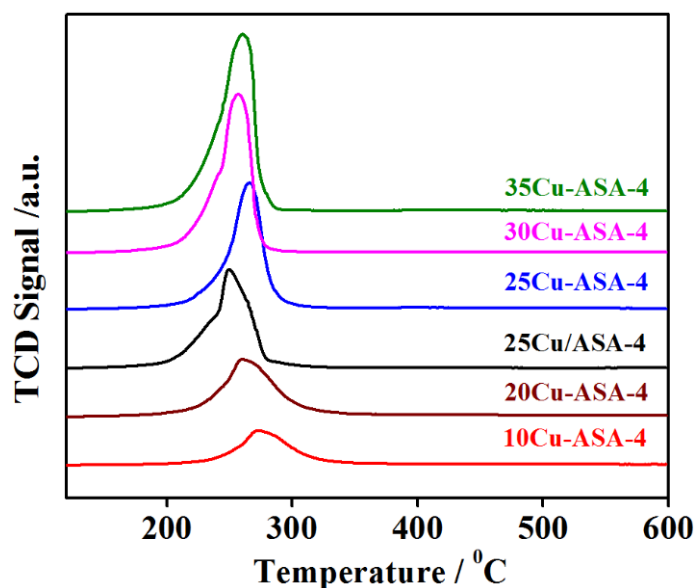


Figure 4. The H₂-TPR profiles of the *x*Cu-ASA-4 and 25Cu/ASA-4 catalysts.

The catalytic results of *x*Cu-ASA-4 for SRD are given in Figure 5. As indicated from the time-on-stream (TOS) data, a volcano shape was ascertained for the changing profile of the initial DME conversion versus the CuO content over the catalysts (Figure 5a), i.e., 25Cu-ASA-4 (~90%) > 30Cu-ASA-4 (~85%) > 20Cu-ASA-4 (~82%) ≈ 35Cu-ASA-4 (~81%) >> 10Cu-ASA-4 (~63%). Moreover, this observation with the same changing order was still applicable for the initial H₂ yields (Figure 5b). With increasing TOS from 1 to 6 h, a minor decrease in the DME conversion was observed for the *x*Cu-ASA-4 catalysts, and the decreased trend was slightly more significant for the TOS H₂ yields except 10Cu-ASA-4 with a sharp decrease. To better understand these phenomena, the selectivity of the carbon-containing products at a TOS of 6 h was calculated. As shown in Figure 5c, the selectivity of CH₄, C₂-C₄ hydrocarbons and CO was very low (<1%) irrespective of the catalysts used. In the case of 10Cu-ASA-4, methanol with a selectivity of about 92% was the main carbon-containing product while the selectivity of CO₂ was only about 7%. This indicates that much less methanol formed via DME hydrolysis was converted during the second-step SRM reaction, leading to the much low efficiency of 10Cu-ASA-4 for the SRD reaction. As a result, the DME conversion of ~60% was still preserved at a TOS of 6 h but the H₂ yield was drastically decreased to be less than 5% (Figure 5a,b). In contrast, methanol was the minor carbon-containing product, and its selectivity at a TOS of 6 h was decreased in the order of 20Cu-ASA-4 (~21%) >> 25Cu-ASA-4 (~8%) ≥ 30Cu-ASA-4 (~7%) ≈ 35Cu-ASA-4 (~7%), indicating that the extent for consuming the methanol intermediate via the SRM reaction was in a reverse order. As (1) the Si/Al molar ratio of ASA for the hydrolysis of DME over the *x*Cu-ASA-4 catalysts was maintained at 4 and (2) Cu⁰ is the active site for the SRM reaction, these SRD results can be reasonably explained if the Cu content and Cu⁰ size are taken into account. This was also supported if the catalytic and characterization results of 25Cu-ASA-4 and 25Cu/ASA-4 were compared, i.e., the clearly higher SRD efficiency and obviously smaller Cu⁰ particles of 25Cu-ASA-4 than those of 25Cu/ASA-4 (~90% and ~40% of the initial H₂ yields vs. 21 and 35 nm of Cu⁰ particles, Figure 5b and Table 1). Moreover, the examination of the initial DME conversion and its TOS changing pattern over *x*Cu-ASA-4 indicated the reciprocal effect between Cu⁰ for SRM and ASA for the DME hydrolysis, i.e., the presence of synergetic effects between the two catalytic functions during SRD. This will be further discussed in detail in Section 2.3.

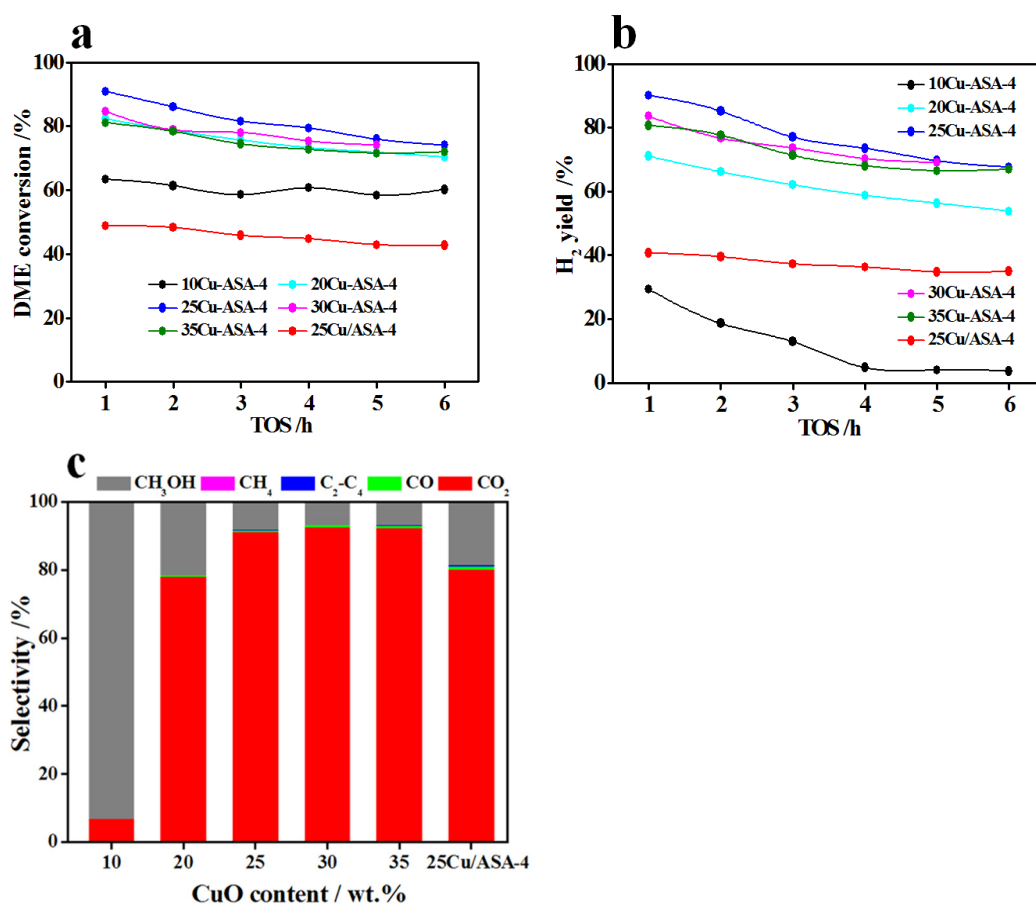


Figure 5. The time-on-stream DME conversion (a), H₂ yield (b), and the selectivity of the carbon-containing products at a TOS of 6 h (c) for the SRD reaction of the x Cu-ASA-4 and 25Cu/ASA-4 catalysts under the conditions of 300 °C, 0.1 MPa, and GHSV of 4000 h⁻¹.

2.2. Effect of Si/Al Molar Ratios

To a certain extent, the acidity of ASA can be commonly regulated by changing the Si/Al ratios provided that the amorphous structure is consistently preserved [16,26]. However, the precursors of Al and Si, the preparation method, and the parameters are important factors in determining the textural and acidic properties of ASA, which essentially originate from the complex arrangements of Si, Al, and O atoms in ASA [11,16,26–29]. As indicated in Figure 6a, almost the same XRD profiles characterizing the amorphous silica and crystalline CuO were still observed irrespective of the Si/Al ratios of the 25Cu-ASA- y catalysts. Moreover, the calculated particle sizes based on the CuO (111) diffraction at 2θ of 35.5° were only slightly dependent on the Si/Al ratio of ASA, i.e., 15–21 nm (Table 1). This was well understandable if the textural properties of the catalysts were examined. As shown in Figure 3b, a typical H4 hysteresis loop for the 25Cu-ASA- y catalysts ($y = 1, 2,$ and 3) was transferred to a clear H3 hysteresis loop for 25Cu-ASA-4 and 25Cu-ASA-5 although a type IV isotherm was still observed for all of these catalysts. This indicates that the pore structures of the 25Cu-ASA- y catalysts ($y = 1, 2$ and 3) varied slightly from those of 25Cu-ASA-4 and 25Cu-ASA-5. As a result, with an increase the Si/Al ratio from 1 to 5, the BET surface area of 25Cu-ASA- y continuously increased from 252.7 to 331.3 m²·g⁻¹ but the total pore volume and average pore size varied only slightly. Since the CuO content of the 25Cu-ASA- y catalysts was kept the same, the slightly smaller CuO size over 25Cu-ASA-4 and 25Cu-ASA-5 can reasonably be ascribed to the higher surface area, which is favorable for dispersing CuO.

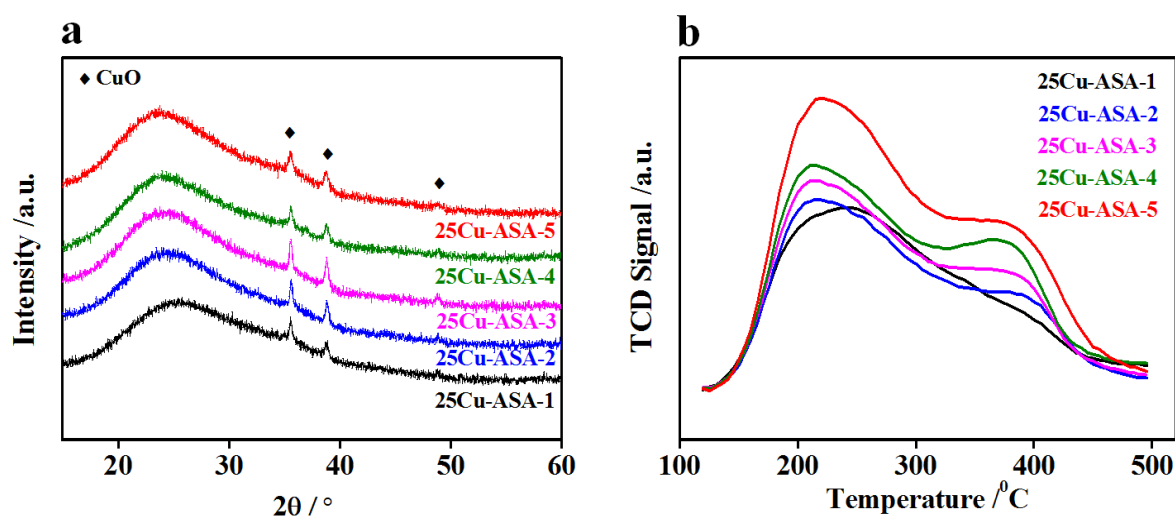


Figure 6. The XRD (a) and NH₃-TPD (b) patterns of the calcined 25Cu-ASA-*y* catalysts.

To estimate the acidity of the 25Cu-ASA-*y* catalysts, NH₃-TPD experiments were performed, and the results are shown in Figure 6b. Irrespective of the Si/Al ratios of the 25Cu-ASA-*y* samples, the pre-adsorbed NH₃ molecules were overwhelmingly desorbed at temperatures ranging from about 150 to 450 °C. In the case of 25Cu-ASA-1, a highly asymmetric and broad peak with a crest temperature of about 240 °C was observed. However, a shoulder at about 380 °C emerged for 25Cu-ASA-2, and its intensity continuously increased with an increase in the Si/Al molar ratio from 2 to 5. These observations indicate the varied distributions of acid sites depending on the Si/Al ratios of 25Cu-ASA-*y*. Following common practice, relatively weaker and stronger acid sites were divided at the temperature of 300 °C based on the characteristics of the NH₃-TPD profiles, and the amount of acid sites was calculated. From the data shown in Table 2, the total amount of acid sites was almost the same over 25Cu-ASA-1 and 25Cu-ASA-2, and it was slightly increased with an increase in the Si/Al ratio from 2 to 5. Where the acidity was concerned, the quantity of weaker acid sites relative to the total amount of acid sites of the 25Cu-ASA-*y* samples was kept almost constant (58 ± 2%) irrespective of the Si/Al ratios, suggesting similar distributions of the Si and Al atoms over the catalysts.

Table 2. The calculated amounts of acid sites of the 25Cu-ASA-*y* catalysts.

Catalyst	Amount of Acid Sites (mmol/g)		
	Total	Weaker	Stronger
25Cu-ASA-1	0.56	0.33	0.23
25Cu-ASA-2	0.55	0.33	0.22
25Cu-ASA-3	0.60	0.35	0.25
25Cu-ASA-4	0.68	0.38	0.30
25Cu-ASA-5	0.86	0.49	0.37

By keeping the same content of CuO for the bifunctional catalysts, the impact of acidity on the performance of 25Cu-ASA-*y* for SRD was determined by adjusting the Si/Al ratios of ASA. From the catalytic results (Figure 7), the SRD reaction for all of the catalysts occurred effectively, and the selectivity of hydrocarbons (CH₄ and C₂-C₄) was very low (less than 0.2%). Moreover, CO₂ was the dominant product, and the selectivity of CO was low (<1%), leading to the high H₂ yield. Specifically, as shown in Figure 7a, the initial DME conversion decreased in the order of 25Cu-ASA-5 (91.1%) ≈ 25Cu-ASA-4 (~89.8%) > 25Cu-ASA-3 (83.9%) > 25Cu-ASA-2 (78.1%) > 25Cu-ASA-1 (72.0%). In the case of the initial H₂ yield (Figure 7b), the change in the order was maintained, i.e., 25Cu-ASA-5 (89.9%) ≈ 25Cu-ASA-4 (~88.9%) > 25Cu-ASA-3 (80.5%) > 25Cu-ASA-2 (71.2%) > 25Cu-ASA-1 (62.0%). If

the difference between the initial DME conversion and H₂ yield was compared, it was significantly decreased with an increase in the Si/Al ratio, i.e., 10% for 25Cu-ASA-1 vs. ~1% for 25Cu-ASA-4 and 25Cu-ASA-5. These results indicate the comparably higher efficiency of SRD for 25Cu-ASA-4 and 25Cu-ASA-5 in the production of hydrogen. This was directly supported by the selectivity of carbon-containing products at a TOS of 6 h (Figure 7c), in which the selectivity of methanol as the main by-product continuously increased in the order of 25Cu-ASA-5 (6.5%) \approx 25Cu-ASA-4 (~7.2%) < 25Cu-ASA-3 (11.8%) < 25Cu-ASA-2 (15.8%) < 25Cu-ASA-1 (19.5%). If the TOS results were examined (Figure 7a,b, a slight and comparable decrease in both the DME conversion and H₂ yield was identified with increasing TOS from 1 to 6 h. If the very similar properties in the aspects of the CuO size, texture, and acidity (Tables 1 and 2) were associated with the SRD results for 25Cu-ASA-1 and 25Cu-ASA-2, the presence of synergetic effects between Cu and acid sites could be perceived, which will be discussed in the next section together with the characterization results of the used catalysts.

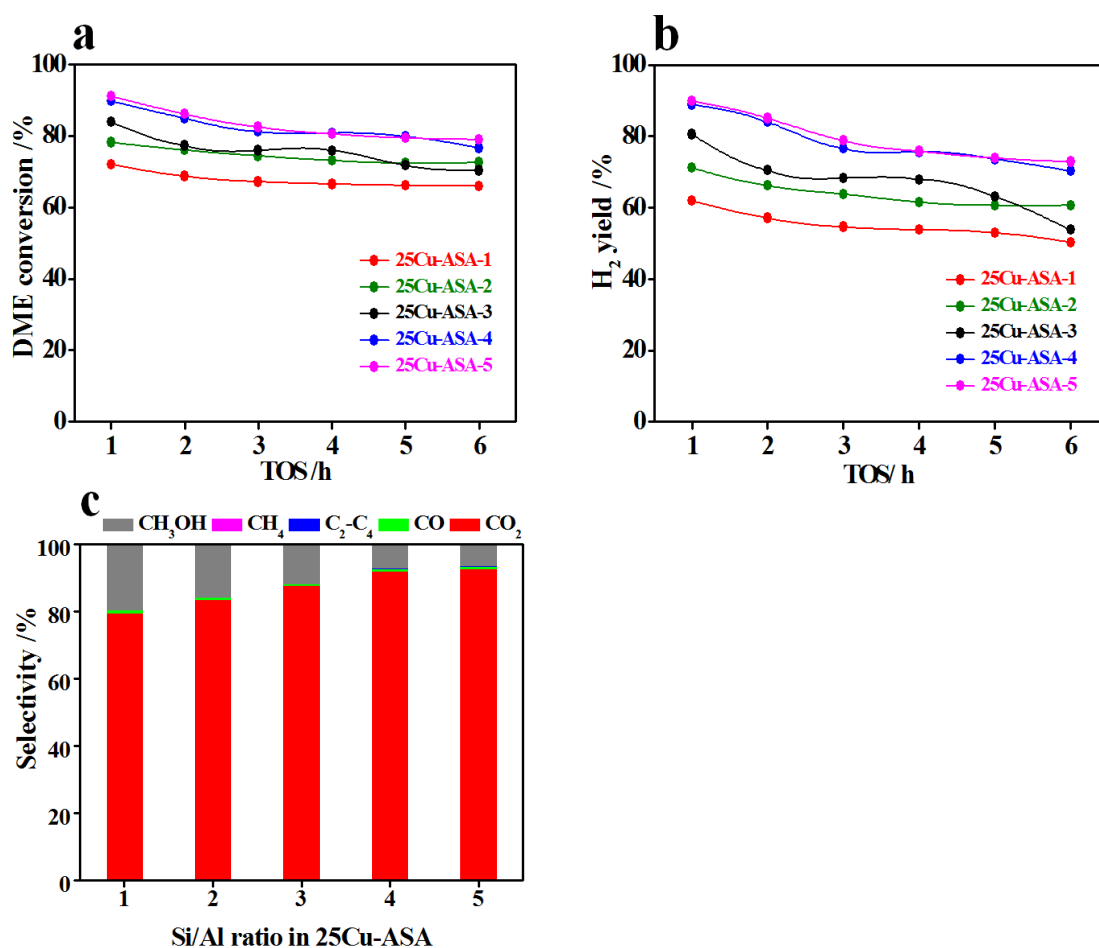


Figure 7. The SRD results for 25Cu-ASA-*y* under the reaction conditions of 300 °C, 0.1 MPa, and GHSV of 4000 h⁻¹. (a) Time-on-stream DME conversions, (b) Time-on-stream H₂ yields, and (c) the selectivity of the carbon-containing products at a TOS of 6 h.

2.3. Insights into the Synergetic Effects

In comparison with the hybrid catalyst, the chemical and structural properties of Cu and the acid sites in the integrated bifunctional catalyst cannot be independently regulated to a relatively larger extent if both a reasonably high DME conversion and H₂ yield are desired. This is exactly the case for the Cu-ASA catalyzed two-step consecutive SRD reaction. Due to the incorporation of Cu into ASA, the most obviously inevitable episode is the advent of inaccessible acid sites over ASA covered by the Cu species, the extent

of which is expected to increase at a higher Cu content of the catalyst. Accordingly, the acid-catalyzed DME hydrolysis (Equation (2)) is reciprocally affected by Cu-catalyzed SRM (Equation (3)) during the SRD reaction of bifunctional Cu–ASA catalysts with various compositions. This analysis is consistent with the SRD results for the $x\text{Cu}$ –ASA– y catalysts.

The synergetic effects between Cu and ASA imposed on the SRD activity can be directly supported if the results for 25Cu/ASA-4 and 25Cu–ASA-4 are comparatively examined. Considering (1) the same synthesis procedure of ASA-4 and 25Cu–ASA-4 and (2) the same compositions and very similar textural properties of the two catalysts (Table 1), analogous kinetics behaviors of 25Cu/ASA-4 and 25Cu–ASA-4 for the DME hydrolysis are reasonably expected. However, great variations between the initial DME conversion (90.9 vs. 48.8%) and H₂ yield (90.0 vs. 40.7%) were observed for the two catalysts (Figure 5). If the two-step nature of the SRD reaction is taken into account, the large difference in the catalytic activity should be induced from varied rates of the second-step reaction of SRD, i.e., SRM. Recalling that Cu⁰ is commonly accepted as the active site for SRM, the SRM rate of 25Cu/ASA-4 is expectedly lower than that for 25Cu–ASA-4 because of the larger Cu⁰ size of 25Cu/ASA-4 compared with 25Cu–ASA-4 (35 vs. 21 nm, Table 1). Thus, the synergetic effects between Cu and ASA play an important role in determining the SRD activity and the H₂ yield. This conclusion is further supported by the results for $x\text{Cu}$ –ASA–4 if both the amount and diameter of Cu⁰ particles are considered. Following this understanding, the results for 25Cu–ASA– y , i.e., the gradually increased MeOH selectivity (Figure 7c), the slightly decreased CuO size (Table 1), and the trivially increased acidity with increasing Si/Al molar ratio, can be explained. Thus, as a result of the two-step consecutive reactions of SRD, the mutual effect between the acid sites for the DME hydrolysis and Cu⁰ for SRM is crucial in determining the activity and H₂ yield of SRD for the Cu–ASA bifunctional catalyst, which is consistent with the results for the hybrid catalysts discussed in our previous work [15].

As shown in Figures 5 and 7, 25Cu–ASA-4 with optimal activity still showed slight decreases in both the DME conversion and H₂ yield when TOS was extended to only 6 h, indicating the lower stability of the $x\text{Cu}$ –ASA– y catalysts. For the Cu-based bifunctional SRD catalysts, the Cu sintering and coking are revealed as the main causes for the catalyst deactivation [1,15,20,22]. To find out the reason, the spent 25Cu–ASA-4 catalyst as a representative was characterized by the TG-DSC technique. As shown in Figure 8a, the weight loss below 150 °C (~5.5%) was due to the removal of the physically adsorbed water, and coke deposited on the catalyst could not be unambiguously determined according to the TG and DSC patterns. However, if the XRD profiles of the reduced and spent 25Cu–ASA-4 catalyst were compared (Figure 8b), the Cu (111) diffraction of the spent catalyst was apparently sharper, indicating the larger Cu⁰ size. This was directly observed from the TEM images, i.e., the larger average Cu⁰ size of 7.3 ± 3.0 nm with a wider distribution of the Cu⁰ particles over the spent catalyst (Figure 8c,d). Thus, the slight decreases in the catalytic activity of SRD over the $x\text{Cu}$ –ASA– y catalysts were mainly caused by Cu sintering, which is agreeable with the findings for the Cu-based hybrid catalysts [22] or the monolithic anodic alumina-supported catalyst of Cu/ γ -Al₂O₃/Al [30]. In contrast, the coke deposition during SRD was revealed as the main reason for the deactivation of the mesoporous-structured Cu-SiO₂-Al₂O₃ catalyst [20]. These results clearly indicate the complicated deactivation behavior of the bifunctional catalysts. If the SRD results of 10Cu–ASA-5 (Figure 5) are analyzed, the significant decrease in the H₂ yield but slight decrease in DME conversion with increasing TOS can be reasonably ascribed as the quick deactivation of Cu in the SRM reaction, which is supported by the very high selectivity of methanol at the end of the test. Thus, the mutual effect of Cu⁰ and acid sites over ASA also play a key role in determining the stability of the bifunctional catalyst, which essentially originated from the consecutive nature of the SRD reaction.

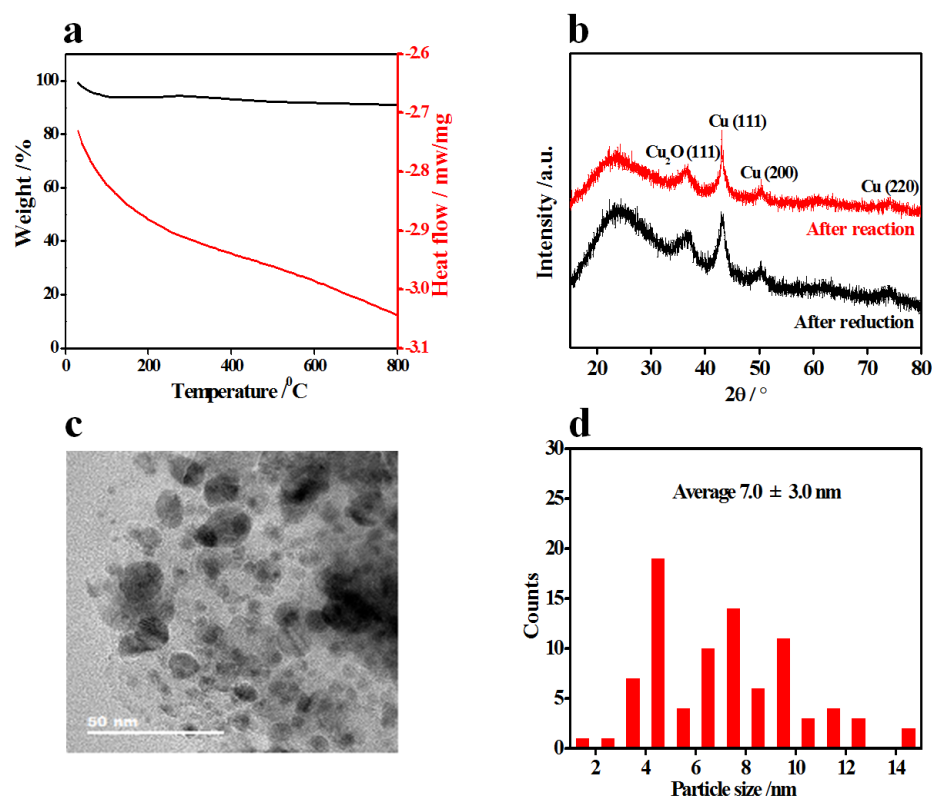


Figure 8. Characterization results of the spent 25Cu-ASA-4 catalyst after SRD for a TOS of 6 h. (a) TG-DSC patterns; (b) XRD profiles of the reduced and used catalyst; (c) TEM image; (d) particle size distribution.

3. Materials and Methods

3.1. Materials

All of the chemicals used in this work, i.e., $\text{Al}(\text{NO}_3)_3 \cdot 9\text{H}_2\text{O}$, $\text{Cu}(\text{NO}_3)_2 \cdot 3\text{H}_2\text{O}$, tetraethoxysilane (TEOS), absolute ethanol, and ammonium carbonate ($(\text{NH}_4)_2\text{CO}_3$), were purchased from Sinopharm Chemical Reagent Co., Ltd., Shanghai, China. The chemicals were directly used without any further treatment.

3.2. Catalyst Preparation

The Cu-ASA samples were synthesized by the single-step complex decomposition method, which is similar to the procedure for synthesizing ASA reported in our previous work [11]. For preparing Cu-ASA catalysts, $(\text{NH}_4)_2\text{CO}_3$ was used as the complex agent while $\text{Al}(\text{NO}_3)_3 \cdot 9\text{H}_2\text{O}$, $\text{Cu}(\text{NO}_3)_2 \cdot 3\text{H}_2\text{O}$, and TEOS were utilized as the precursor of Cu, Si, and Al, respectively. Firstly, the desired amount of $\text{Cu}(\text{NO}_3)_2 \cdot 3\text{H}_2\text{O}$ and $\text{Al}(\text{NO}_3)_3 \cdot 9\text{H}_2\text{O}$ were dissolved in 40 mL absolute ethanol in a beaker and stirred for 20 min at room temperature. To the solution, the required amount of TEOS was slowly added under vigorous stirring for 40 min. After slowly adding the $(\text{NH}_4)_2\text{CO}_3$ aqueous solution (the molar ratio of $(\text{NH}_4)_2\text{CO}_3 / (\text{Si} + \text{Al}) = 0.5$ for all of the syntheses), it was further stirred at room temperature for 10 min. Subsequently, the beaker was sealed with a polyethylene film and kept at 60 °C under stirring until a viscous gel was formed. After the gel was transferred to a porcelain vessel, it was rapidly burnt for 10 min in an electric furnace. Finally, Cu-ASA catalysts with different compositions were obtained after calcining in air under the same conditions, i.e., from room temperature to 550 °C at a ramp rate of $5\text{ °C} \cdot \text{min}^{-1}$ and kept at 550 °C for 4 h. The final catalysts were denoted as $x\text{Cu-ASA-}y$, where x and y represent the CuO content ($x = 10, 20, 25, 30,$ and 35 wt.%) and Si/Al molar ratios ($y = 1, 2, 3, 4,$ and 5), respectively.

Following the same procedure but without the addition of the Cu precursor, ASA with a Si/Al molar ratio of 4 was synthesized. After loading 25 wt.% CuO via the impregnation method, the catalyst was named 25Cu/ASA-4.

3.3. Procedure for Evaluating the SRD Performance

The catalytic SRD reaction was carried out in a quartz tube reactor (i.d. = 6.0 mm). All of the tests were performed by using 0.6 g of each catalyst, which was pulverized and sieved through 40–60 mesh. Prior to the reaction, the catalysts were reduced at 300 °C for 0.5 h in mixed gases of 10 vol.% H₂/N₂. After this, the SRD reaction was performed under the same conditions of DME/H₂O/N₂ with a fixed molar ratio of 1/4/5, 0.1 MPa, 300 °C, gas hourly space velocity (GHSV) of 4000 h⁻¹, and time-on-stream (TOS) of 6 h. The exits were analyzed online on a gas chromatograph equipped with both a thermal conductivity detector (TCD) and a flame ionization detector (FID). For the detailed reaction procedure, the analyses of the products, and the calculation methods, please see our previous publication [1].

3.4. Catalyst Characterization

The powder X-ray diffraction (XRD) patterns of samples were collected on a Bruker advanced D8 X-ray diffraction meter using Cu K α ($\lambda = 0.154$ nm) generated at 40 kV and 20 mA.

The textural properties of the samples were determined by N₂ adsorption/desorption measurements at -196 °C on a Micromeritics ASAP 2020 instrument. Before N₂ adsorption/desorption, each sample (ca. 100 mg) was degassed under vacuum at 300 °C for 12 h. The Brunauer–Emmett–Teller (BET) method was applied to determine the specific surface area, and the total pore volume was calculated until a relative pressure (P/P_0) of 0.99.

The temperature-programmed reduction in hydrogen (H₂-TPR) was performed on a Micromeritics Autochem 2920 instrument. Firstly, the catalyst (100 mg) was treated at 400 °C for 30 min under a flow of pure Ar (30 mL min⁻¹). After it was cooled to room temperature, 10 vol.% H₂/Ar with a flow rate of 30 mL min⁻¹ was used and stabilized for 30 min. Finally, the H₂-TPR was performed from room temperature to 600 °C at a ramp rate of 10 °C/min while the hydrogen consumption was simultaneously monitored by TCD.

Transmission electron microscopy (TEM) and high-resolution TEM (HRTEM) were applied to directly observe the representative catalysts, the images of which were obtained on an FEI Tecnai G2-F20 instrument operated at 200 kV.

The acidity of the ASA-4 and x Cu-ASA- y catalysts was measured by the temperature-programmed desorption of ammonia (NH₃-TPD) on a Micromeritics Auto 2920 instrument. The consecutive procedure and conditions before the NH₃-TPD experiment were as follows, i.e., sample loading of 500 mg, the removal of any volatiles at 500 °C in pure helium for 1 h, the adsorption of ammonia at 120 °C for 0.5 h with a 20 mL·min⁻¹ flow of diluted NH₃, and the removal of the physically adsorbed NH₃ at 120 °C for 2 h under pure helium flow. Desorbed ammonia was monitored with a TCD, and the NH₃-TPD pattern was recorded from 120 to 500 °C (10 °C·min⁻¹) under pure helium flow (25 mL·min⁻¹).

The thermogravimetric and differential scanning calorimetry (TG-DSC) analyses of the representatively used catalyst were carried out on a Q1000DSC + LNCS + FACS Q600SDT instrument by loading 20 mg of the sample in the crucible. The TG-DSC profiles were recorded in an air atmosphere when the temperature increased from room temperature to 800 °C at a heating rate of 10 °C min⁻¹.

4. Conclusions

With the use of ammonium carbonate as the coordinating agent, the single-step complex decomposition method was revealed to be effective for synthesizing ASA and dispersing CuO in ASA with largely varied compositions. In comparison with 25Cu/ASA-4 prepared by the impregnation method, 25Cu-ASA-4 with the same composition yielded much smaller sizes of CuO and Cu⁰ particles. When the CuO content was increased from

10 to 35 wt.%, the Cu⁰ sizes over the reduced xCu–ASA-4 catalysts continuously increased from 12 to 33 nm. Moreover, even if the Si/Al molar ratio of 25Cu–ASA-y was increased from 1 to 5, the textural properties, diameter of the CuO particles, and the acidity of the catalysts were slightly varied, and the amount of weaker acid sites relative to that of the total acid sites was kept almost constant at 58 ± 2%. The initial DME conversion and H₂ yield higher than 90% were achieved at 300 °C for SRD compared with the optimal 25Cu–ASA-4 catalyst. Depending on the composition of xCu–ASA-y, the SRD performance decreased with increasing TOS to different extents, the reason of which was revealed as Cu sintering. The correlation of the reaction and characterization results revealed that the synergetic effect between ASA and Cu played a crucial role in determining the activity, H₂ yield, and stability of the integrated Cu–ASA bifunctional catalyst for SRD. Thus, a more active and stable SRD catalyst is reasonably expected if the sintering of Cu over the optimized 25Cu–ASA-4 catalyst can be greatly inhibited, e.g., by adding a promoter such as ZnO or noble metals including Pd, which is worthy of investigation.

Author Contributions: Conceptualization, Z.-W.L.; formal analysis, Z.-W.L., Z.-C.S., L.W. and C.L.; investigation, Z.-C.S. and M.-L.Z.; data curation, Z.-C.S.; writing—original draft preparation, Z.-W.L., Z.-C.S. and L.W.; writing—review and editing, Z.-W.L.; supervision, Z.-W.L. All authors have read and agreed to the published version of the manuscript.

Funding: National Natural Science Foundation of China (U1862116) and Fundamental Research Funds for the Central Universities (GK201901001).

Conflicts of Interest: The authors declare no conflict of interest.

References

1. Li, J.; Zhang, Q.-J.; Long, X.; Qi, P.; Liu, Z.-T.; Liu, Z.-W. Hydrogen production for fuel cells via steam reforming of dimethyl ether over commercial Cu/ZnO/Al₂O₃ and zeolite. *Chem. Eng. J.* **2012**, *187*, 299–305. [[CrossRef](#)]
2. Takeishi, K.; Suzuki, H. Steam reforming of dimethyl ether. *Appl. Catal. A Gen.* **2004**, *260*, 111–117. [[CrossRef](#)]
3. Sobyenin, V.A.; Cavallaro, S.; Freni, S. Dimethyl Ether Steam Reforming to Feed Molten Carbonate Fuel Cells (MCFCs). *Energy Fuels* **2000**, *14*, 1139–1142. [[CrossRef](#)]
4. Galvita, V.V.; Semin, G.L.; Belyaev, V.D.; Yurieva, T.M.; Sobyenin, V.A. Production of hydrogen from dimethyl ether. *Appl. Catal. A Gen.* **2001**, *216*, 85–90. [[CrossRef](#)]
5. Sun, Z.; Tian, Y.; Zhang, P.; Yang, G.; Tsubaki, N.; Abe, T.; Taguchi, A.; Zhang, J.; Zheng, L.; Li, X. Sputtered Cu-ZnO/γ-Al₂O₃ Bifunctional Catalyst with Ultra-Low Cu Content Boosting Dimethyl Ether Steam Reforming and Inhibiting Side Reactions. *Ind. Eng. Chem. Res.* **2019**, *58*, 7085–7093. [[CrossRef](#)]
6. Kim, D.; Choi, B.; Park, G.; Lee, K.; Lee, D.-W.; Jung, S. Effect of γ-Al₂O₃ characteristics on hydrogen production of Cu/γ-Al₂O₃ catalyst for steam reforming of dimethyl ether. *Chem. Eng. Sci.* **2020**, *216*, 115535. [[CrossRef](#)]
7. Takeishi, K.; Akaike, Y. Hydrogen production by dimethyl ether steam reforming over copper alumina catalysts prepared using the sol-gel method. *Appl. Catal. A Gen.* **2016**, *510*, 20–26. [[CrossRef](#)]
8. Semelsberger, T.A.; Ott, K.C.; Borup, R.L.; Greene, H.L. Generating hydrogen-rich fuel-cell feeds from dimethyl ether (DME) using physical mixtures of a commercial Cu/Zn/Al₂O₃ catalyst and several solid-acid catalysts. *Appl. Catal. B Environ.* **2006**, *65*, 291–300. [[CrossRef](#)]
9. Vicente, J.; Gayubo, A.G.; Ereña, J.; Aguayo, A.T.; Olazar, M.; Bilbao, J. Improving the DME steam reforming catalyst by alkaline treatment of the HZSM-5 zeolite. *Appl. Catal. B Environ.* **2013**, *130–131*, 73–83. [[CrossRef](#)]
10. Faungnawakij, K.; Eguchi, K. Dimethyl Ether-Reforming Catalysts for Hydrogen Production. *Catal. Surv. Asia* **2010**, *15*, 12–24. [[CrossRef](#)]
11. Shao, Z.-C.; Liu, C.; Xiao, Y.-S.; Wang, L.; Liu, Z.-T.; Liu, Z.-W. Texture and acidity of amorphous silica-alumina regulated by the complex-decomposition method for steam reforming of dimethyl ether. *Catal. Today* **2022**, *402*, 172–182. [[CrossRef](#)]
12. Halasi, G.; Bánsági, T.; Solymosi, F. Production of Hydrogen from Dimethyl Ether over Supported Rhodium Catalysts. *ChemCatChem* **2009**, *1*, 311–317. [[CrossRef](#)]
13. Ramos, E.; Davin, L.; Angurell, I.; Ledesma, C.; Llorca, J. Improved Stability of Pd/Al₂O₃ Prepared from Palladium Nanoparticles Protected with Carbosilane Dendrons in the Dimethyl Ether Steam Reforming Reaction. *ChemCatChem* **2015**, *7*, 2179–2187. [[CrossRef](#)]
14. Solymosi, F.; Barthos, R.; Kecskeméti, A. The decomposition and steam reforming of dimethyl ether on supported Mo₂C catalysts. *Appl. Catal. A Gen.* **2008**, *350*, 30–37. [[CrossRef](#)]
15. Long, X.; Song, Y.-H.; Liu, Z.-T.; Liu, Z.-W. Insights into the long-term stability of the magnesia modified H-ZSM-5 as an efficient solid acid for steam reforming of dimethyl ether. *Int. J. Hydrog. Energy* **2019**, *44*, 21481–21494. [[CrossRef](#)]

16. Wang, S.-S.; Song, Y.-H.; Zhao, Y.-H.; Liu, C.; Xiao, Y.-S.; Zhang, Q.; Liu, Z.-T.; Liu, Z.-W. Amorphous silica-alumina composite with regulated acidity for efficient production of hydrogen via steam reforming of dimethyl ether. *Catal. Today* **2020**, *351*, 68–74. [[CrossRef](#)]
17. Ledesma, C.; López, E.; Trifonov, T.; Rodríguez, Á.; Llorca, J. Catalytic reforming of dimethyl ether in microchannels. *Catal. Today* **2019**, *323*, 209–215. [[CrossRef](#)]
18. Ranjekar, A.M.; Yadav, G.D. Steam Reforming of Methanol for Hydrogen Production: A Critical Analysis of Catalysis, Processes, and Scope. *Ind. Eng. Chem. Res.* **2021**, *60*, 89–113. [[CrossRef](#)]
19. Nadeina, K.A.; Klimov, O.V.; Danilova, I.G.; Pereyema, V.Y.; Gerasimov, E.Y.; Prosvirin, I.P.; Noskov, A.S. Amorphous silica-alumina-perspective supports for selective hydrotreating of FCC gasoline: Influence of Mg. *Appl. Catal. B Environ.* **2018**, *223*, 22–35. [[CrossRef](#)]
20. Zang, Y.-H.; Dong, X.-F.; Wang, C.-X. One-pot synthesis of mesoporous Cu-SiO₂-Al₂O₃ bifunctional catalysts for hydrogen production by dimethyl ether steam reforming. *Chem. Eng. J.* **2017**, *313*, 1583–1592. [[CrossRef](#)]
21. Zhao, S.; Yue, H.-R.; Zhao, Y.-J.; Wang, B.; Geng, Y.-C.; Lv, J.; Wang, S.-P.; Gong, J.-L.; Ma, X.-B. Chemoselective synthesis of ethanol via hydrogenation of dimethyl oxalate on Cu/SiO₂: Enhanced stability with boron dopant. *J. Catal.* **2013**, *297*, 142–150. [[CrossRef](#)]
22. Wang, X.-L.; Ma, K.; Guo, L.-H.; Tian, Y.; Cheng, Q.-P.; Bai, X.-Q.; Huang, J.-J.; Ding, T.; Li, X.-G. Cu/ZnO/SiO₂ catalyst synthesized by reduction of ZnO-modified copper phyllosilicate for dimethyl ether steam reforming. *Appl. Catal. A Gen.* **2017**, *540*, 37–46. [[CrossRef](#)]
23. Thommes, M.; Kaneko, K.; Neimark, A.V.; Olivier, J.P.; Rodriguez-Reinoso, F.; Rouquerol, J.; Sing, K.S.W. Physisorption of gases, with special reference to the evaluation of surface area and pore size distribution (IUPAC Technical Report). *Pure Appl. Chem.* **2015**, *87*, 1051–1069. [[CrossRef](#)]
24. Zhu, Y.-F.; Kong, X.; Li, X.-Q.; Ding, G.-Q.; Zhu, Y.-L.; Li, Y.-W. Cu Nanoparticles Inlaid Mesoporous Al₂O₃ As a High-Performance Bifunctional Catalyst for Ethanol Synthesis via Dimethyl Oxalate Hydrogenation. *ACS Catal.* **2014**, *4*, 3612–3620. [[CrossRef](#)]
25. Unutulmazsoy, Y.; Cancellieri, C.; Lin, L.; Jeurgens, L.P.H. Reduction of thermally grown single-phase CuO and Cu₂O thin films by in-situ time-resolved XRD. *Appl. Surf. Sci.* **2022**, *588*, 152896. [[CrossRef](#)]
26. Escribano, V.S.; Garbarino, G.; Finocchio, E.; Busca, G. γ -Alumina and Amorphous Silica-Alumina: Structural Features, Acid Sites and the Role of Adsorbed Water. *Top. Catal.* **2017**, *60*, 1554–1564. [[CrossRef](#)]
27. Toyama, N.; Umegaki, T.; Kojima, Y. Influence of Si/Al molar ratio of hollow silica-alumina composite spheres on their activity for hydrolytic dehydrogenation of ammonia borane. *Int. J. Hydrog. Energy* **2015**, *40*, 6151–6157. [[CrossRef](#)]
28. Larmier, K.; Chizallet, C.; Maury, S.; Cadran, N.; Abboud, J.; Lamic-Humblot, A.F.; Marceau, E.; Lauron-Pernot, H. Isopropanol Dehydration on Amorphous Silica-Alumina: Synergy of Bronsted and Lewis Acidities at Pseudo-Bridging Silanols. *Angew. Chem. Int. Ed.* **2017**, *56*, 230–234. [[CrossRef](#)]
29. Li, T.; Tao, Z.; Hu, C.; Zhao, C.; Yi, F.; Zhao, G.; Zhang, L.; Yang, Y. Brønsted acidity of amorphous silica-aluminas for hydrocracking of Fischer-Tropsch wax into diesel fractions. *Appl. Catal. A Gen.* **2022**, *630*, 118439. [[CrossRef](#)]
30. Zhang, Q.; Xu, J.; Fan, F.; Sun, D.; Xu, G.; Zhang, S.; Zhu, Z. Application of porous anodic alumina monolith catalyst in steam reforming of dimethyl ether: Cu/ γ -Al₂O₃/Al catalyst degradation behaviors and catalytic activity improvement by pre-competition impregnation method. *Fuel Process. Technol.* **2014**, *119*, 52–59.